

Macroscopic bubble generation promoted by nanobubble seeds as a traceless anti-fluctuation strategy for water splitting

Received: 2 September 2024

Accepted: 13 June 2025

Published online: 01 July 2025

 Check for updatesSheng Yang, Jing Yuan, Pengpeng Xie, Bo Li, Mengxuan Li, Daojin Zhou ,
Liang Luo  & Xiaoming Sun  

To adapt fluctuating renewable energy for water splitting is challenging, since the growth of electrochemically generated nanobubbles at early stage requires high supersaturation during the repeated start-stop cycles, which can accelerate the deactivation of electrodes and cause extra energy consumption. Herein, we propose a “bubble seeding” strategy by introducing nanobubbles (NBs, ~200 nm in diameter) into electrolyte to promote the generation of macroscopic bubbles. The precursive nanobubbles can act as the beforehand nuclei with a certain supersaturation, lower the supersaturation barrier for further growth, and result in reduced overpotential as high as 130 mV for oxygen evolution reaction. The enhancement depends on nanobubble coverage and size, with higher coverage and larger sizes favoring macrobubble growth. The nanobubbles with inert gas species (e.g. N₂ for oxygen evolution reaction) can also work as the seeds, while the interfering or consumable gas species (e.g. O₂ for hydrogen evolution reaction) would hinder the generation of macroscopic bubbles and enlarge the overpotential. The water splitting device working at presence of nanobubbles exhibits stable operation voltage during repeated start-stop cycles in contrast to traditional electrolyte without NBs, indicating great potential of such traceless nanobubble additive strategy for stabilizing gas evolution applications.

Production of green hydrogen via renewable energy-based water splitting is a promising route to achieve the carbon peak and neutrality goals^{1–4}. The capacity of renewable energy, such as wind and solar power, has been sharply increased in the last decade. There comes an emerging issue: how to adapt to the fluctuation of renewable energy sources?^{5,6} Currently, water splitting devices are usually operated under constant working conditions with the integration of smart electricity grids or power plants^{7–10}. However, with the explosive development of sustainable energy supply, water splitting systems themselves should be designed with well adaptability to the fluctuation, which still lacks systematic investigation.

The optimization remains largely unexplored due to the lack of understanding of a thorough bubble evolution process^{11–13}, which usually starts from the heterogeneous nucleation of nanobubbles (NBs)^{14–21}, ends up with the detachment of macroscopic bubbles (MBs) from electrodes^{22–27}. For the scenarios of large current densities, the attachment of macrobubbles, on one hand, can decrease electrocatalytic surface, causing additional transport overpotential^{28–31}; and on the other hand, the departure of macrobubbles would induce local convection, relieving supersaturation near the electrode^{32,33}. To this context, regulating bubble behavior is highly desired and rigorously perused to enhance the overall performance of the steady-state operation of the water splitting device. Traditional efforts of bubble

State Key Laboratory of Chemical Resource Engineering, College of Chemistry, Beijing University of Chemical Technology, Beijing, China.

 e-mail: luoliang@mail.buct.edu.cn; sunxm@mail.buct.edu.cn

engineering have been made mainly focusing on electrode design (e.g., composition, structures)^{34–38}, and flow channels^{39–41}. While for the start-up stage, the MBs formation would experience the nucleation of NBs and their further growth from NBs^{42,43}, which directly relates to the performance of start-stop operations, but bubble engineering at this dimension is still overlooked.

The transformation from NBs to MBs requires a unique high supersaturation to overcome the internal pressure inside NBs owing to their ultra-small size according to the Young–Laplace equation ($\Delta p = 2\gamma/r$), where γ is the surface tension, r is the bubble radius⁴³. Very recently, our investigation of NBs’ “pin-rise” model revealed that the curvature radius of NB decreases with increasing contact angle and height, and pinned three-phase boundaries during the initial growth stage (Fig. 1a)⁴⁴. The further growth of NBs needs to overcome the critical contact angle or curvature radius to de-pin (extend) the three-phase boundaries for the subsequent transformation to MBs, which requires high enough supersaturation to overcome the internal pressure inside NBs^{45,46}. The built-up of supersaturation with NB pinning would become a problem during the start-up stage, accelerating electrode fading and even hydrogen embrittlement, which cannot be neglected as usual.

To this end, we propose a “bubble-seeding” strategy to promote the generation of MBs by introducing suspending NBs into the electrolyte. By adsorbing on the electrode surface, the introduced NBs can act as the seeding big nucleus to lower the supersaturation barrier for further growth, resulting in reduced overpotential (Fig. 1b). Besides, such seeds can be the productive gas (e.g., O₂ for OER) NBs for practical devices, which would be transformed to MBs, without interfering with the purity of final products. Such traceless “NB additive” strategy demonstrated its versatility by using various productive or inert reaction gas species (e.g., N₂ for HER and OER). The stability of the water splitting device after repeated start-stop cycles indicates great potential of such NB additive strategy for gas evolution applications.

Results and discussion

Initial assessment of the “bubble-seeding” strategy

To investigate the promotion effect of bulk NBs for macrobubble evolution, a three-electrode setup consisting of the as-prepared Pt/Au electrode (Fig. S1) as the working electrode, a Pt plate as the counter electrode, and Hg/HgO as the reference electrode, was used to conduct the electrochemical tests. The bulk NB solution was prepared via a NB generator by shearing force, and the clear Tyndall effect under an incident laser beam indicates the existence of NBs in the transparent solution (Fig. S2a). The number concentration of NBs was evaluated by nanoparticle tracking analysis (NTA) as 10⁸ particles/mL, which is three exponentials higher than the control samples of deionized water (3 × 10⁵ particles/mL) and oxygen-saturated water (6 × 10⁵ particles/mL), and the average size of NBs is ~200 nm in diameter (Fig. S2b). No performance variation of Pt/Au electrode was observed during linear sweep voltammetry (LSV) testing and cyclic voltammetry (CV) testing (Fig. S3), eliminating the possibility of surface reconstruction of the electrode during electrochemical testing⁴⁷.

As presented in Fig. 1c, by introducing NBs to the electrolyte, the OER onset potential of the Pt/Au electrode at the current density of 1 mA/cm² is found to be 1.70 V (vs RHE), with a lowered overpotential ($\Delta\eta$) of 130 mV relative to the intrinsic onset potential (1.83 V) without bulk NBs. To further verify such promotion effect, a small amount of bulk NB solution (5 mL) was injected into the electrolyte (25 mL) at the equilibrium state (400 s) of OER at a rather limited potential of 1.7 V (vs RHE). As shown in Fig. 1d, there is an obvious current jump after the injection of bulk oxygen NBs solution, accompanied by the appearance of MBs on the electrode (Fig. 1d inset), while no observable current change after the injection of oxygen-saturated solution, which is

similar to the control experiment without injection. Such a phenomenon can be solely attributed to the addition of NBs, rather than the convection induced by the injection. Besides, the promotion effect is sustained when NBs are continuously injected into the cell (Fig. S4). As a result, the introduction of bulk NBs can effectively lower the onset potential of OER, as a “traceless” additive to promote the gas evolution reaction.

The influence of NBs’ coverage

The adsorption process of NBs on the flat Pt/Au electrode surface without applying voltage was visualized with real-time surface plasmon resonance imaging (SPRI) technique, which is extremely sensitive to the dielectric field change near the 50 nm Pt/Au film, and has been a powerful tool to investigate surface chemistry^{44,48,49}. As shown in Fig. 2a, accompanied by the typical NB adsorption process, the differential images of SPRI become more and more brightened (from black to gray) from 0 to 180 s, and the contrast remains constant afterward. Accordingly, with the NB adsorption, the SPR reflectivity increases from 0 to a plateau of ~2.6%, indicating the adsorption equilibrium after 200 s. The results suggest that the surface adsorption of bulk NBs would approach an equilibrium state in a short time (<240 s), and the surface coverage would remain constant after this period.

Atomic force microscopy (AFM) test was further conducted on a Pt/Au electrode within a 3 × 3 μm² area to evaluate the morphology of NBs after the adsorption equilibrium (Fig. 2b). The AFM image (Fig. S5) verifies that the as-prepared Pt/Au electrode is smooth ($R_a = 0.897$ nm), and the adsorbed NBs are found to be with the contact angle of ~10–40° (Figs. S6–S8). Based on the verification of AFM images, the coverage-reflectivity relation can be established, similar to our reported results⁴⁴.

By adjusting the adsorption time before OER tests, we found that the onset potential at 1 mA/cm² shifts from 1.76 V to 1.70 V with increasing adsorption time (without adsorption of NBs, the onset potential is 1.83 V), verifying the promotion effect of introducing NBs (Fig. 2c). As taking a different perspective for such variation, the current density at the potential of 1.75 V (vs RHE) increases accordingly with the prolonging of NB adsorption time (Fig. 2d). For the scenario with intrinsic nucleation, the current density is rather limited, as low as 0.17 mA/cm² (black line). According to our reported result⁴⁴, the typical growth of NBs would probably follow a “constant contact diameter” model, and the formed NB nucleus keeps the pinning state before the formation of MBs. As the internal pressure of NBs is much higher than the ambient pressure, as estimated by Young–Laplace equation ($\Delta P = 2\gamma/r$), there would be corresponding supersaturated environments nearby, regarded as the concentration of NB surface (C_s), as expressed by,

$$C_s = \frac{1}{k_H} \left(P_0 + \frac{2\sigma}{r} \right) \quad (1)$$

where P_0 is the ambient pressure, σ is the surface tension. According to Henry’s law, namely $P_{NB} = k_H \times C_s$, where k_H is Henry’s coefficient. And the outflux from NBs to the bulk phase is balanced with the influx of electrochemically generated H₂ molecules. Thus, the electrochemical reaction nearby NBs would undergo in a supersaturated environment, and further transformation from NB to MB requires a higher threshold (e.g., higher gas concentration) during the NB pinning process, since the chemical potential of NBs would increase with their decreasing curvature radius. While for the scenarios with adsorbed NBs as given nucleus (~130 nm in curvature radius, Fig. S8), which are commonly larger in size than the intrinsically formed ones (~72 nm) reported in our previous work⁴⁵, namely, larger curvature radius r . Thus, the supersaturation nearby the adsorbed NBs would be lower than that of the intrinsic nucleus. As OER is rather a kinetic irreversible reaction, we

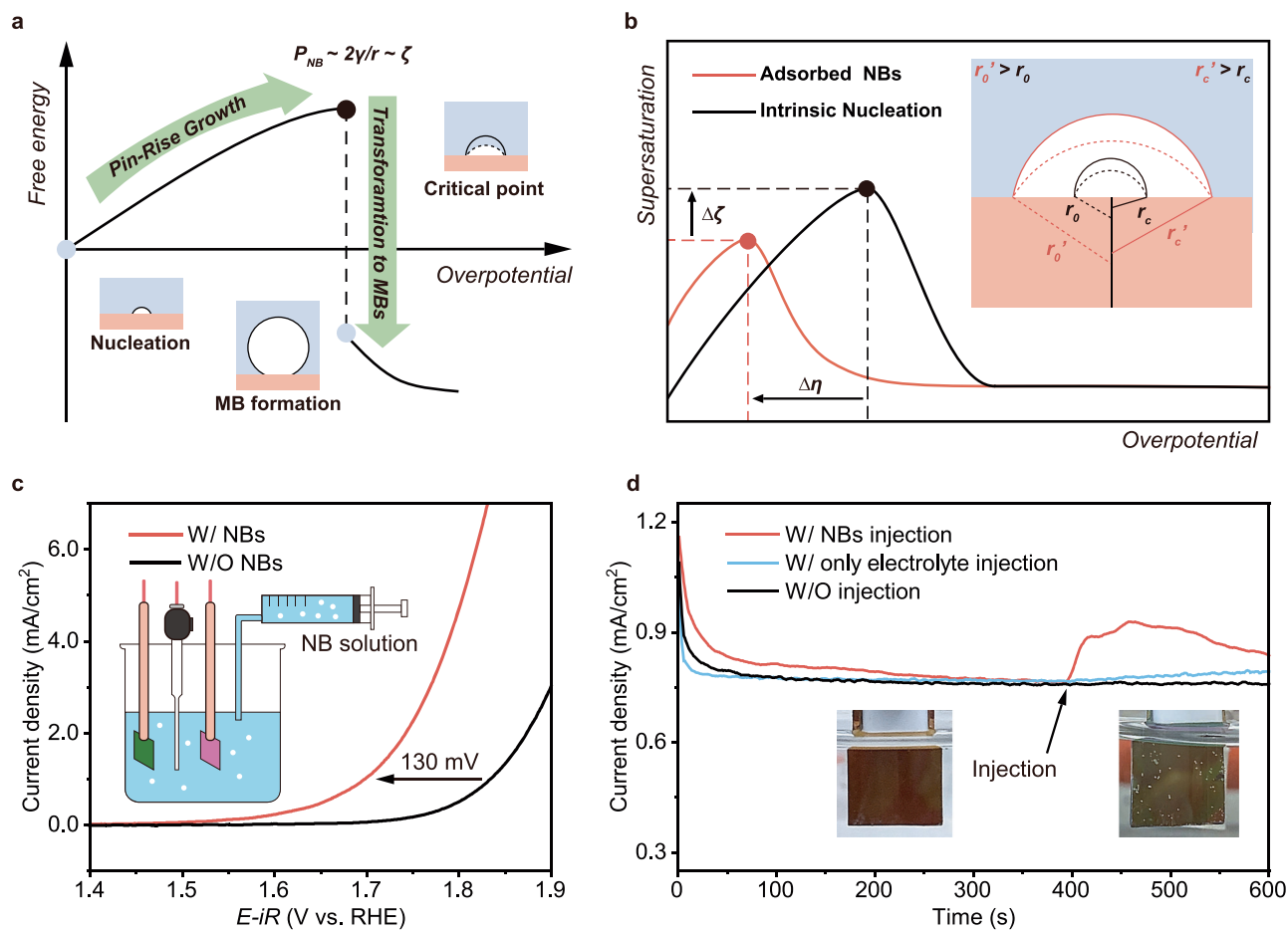


Fig. 1 | NBs as a traceless additive to promote gas evolution reactions. **a** Pin-rise growth of surface nanobubbles during the initial stage of gas evolution reaction. **b** Scheme of the relation between the supersaturation nearby the intrinsic generated (black), adsorbed (red) surface NBs and the overpotential during gas phase transformation. **c** OER polarization curves of the Pt/Au electrode (1 × 1 cm²) with (red) and without (black) the introduction of NBs (with 100% iR correction and

$R_s = 3.62 \Omega$ for W/NBs and 3.73Ω for W/O NBs. The non- iR corrected voltammograms are provided in Supplementary Fig. S30). **d** Current density variations at 1.7 V (vs RHE) after the injections of NB solution (red), electrolyte-only (blue), respectively, and without injection (black) (working area: 1.5×1.5 cm²). Source data for (c, d) are provided as a Source Data file.

did not attribute the promotion effect to the OER concentration overpotential^{12,50–53}. Besides, as the adsorbed NBs can transform to MBs at an earlier stage of gas evolution reaction, the enhanced local convection during the MB growth would further facilitate mass transfer, resulting in a promotion effect, coinciding with the phenomenon in Fig. 1c, d^{23,30}.

We further conducted surface plasmon resonance microscope (SPRM)^{48,54} to observe the growth/detachment of processes at a potential of -0.58 V vs RHE (Fig. S9). As shown in Fig. 2e and Supplementary Movie 1, at 1.35 s, a macrobubble approached its critical size for detachment. After 50 ms (1.40 s), a gas nucleus with a size of $\sim 10 \mu\text{m}$ remained. At this stage, even though the adsorbed NBs have transformed to macrobubbles, the gas nuclei at macroscale that remained could still act as the generation site for the growth of the next macrobubbles (7.65 and 13.70 s). Since this is a buoyancy-driven bubble departure process, the inevitable roughness/defects on the Pt/Au electrode would serve as the pinning sites of the macrobubble. Upon departure, buoyancy and the adhesion force would induce a bubble neck, which results in the incomplete departure of the macrobubble, leaving the gas nuclei^{55,56}. We elucidate that the adsorbed NBs can not only serve as the nuclei for the growth of MBs, but also help to form gas seeds for the successive growth of MBs after their detachment (Figs. 2e and S10).

The influence of NBs' size

Besides, the size influence is also critical for such promotional effect. Different-sized bulk NBs were acquired by placing the freshly generated NB solution for different times. As shown in Fig. 3a, the average diameter of freshly generated NBs is ~ 235 nm and increases to ~ 290 nm within 10 h. Accordingly, the number density of the NB solution decreases from $\sim 11.0 \times 10^7$ particles/mL to 3.10×10^7 particles/mL. Such different-sized NBs were diluted to maintain a number density of $\sim 3 \times 10^7$ and further introduced into the electrolyte for the adsorption, and the equilibrium coverages were found to be essentially the same, as evidenced by the reflectivity of $2.5 \pm 0.1\%$ SPRi after 240 s (Fig. S11). As shown in Fig. 3b, the corresponding polarization curves indicated that the OER onset potential decreases with the increase of the introduced NB size. Like the trend of NB coverage, the current density also exhibits a positive correlation with r at the overpotential of 1.75 V. Also, the OER potential shifts from 1.76 to 1.73 V at the current density of 0.4 mA/cm² as the average r increases from 225 to 291 nm. Further calculation demonstrates that the OER overpotential decreases with decreasing adsorbed NB supersaturation ratio (Fig. 3c). In other words, the required critical overpotential for the transformation from NBs to MBs decreases with the increase of the introduced NBs' size. As mentioned above, the further growth of the NB nucleus to MBs is to overcome the critical contact angle (or curvature radius) for depinning the three-phase boundaries, and the critical contact angle is

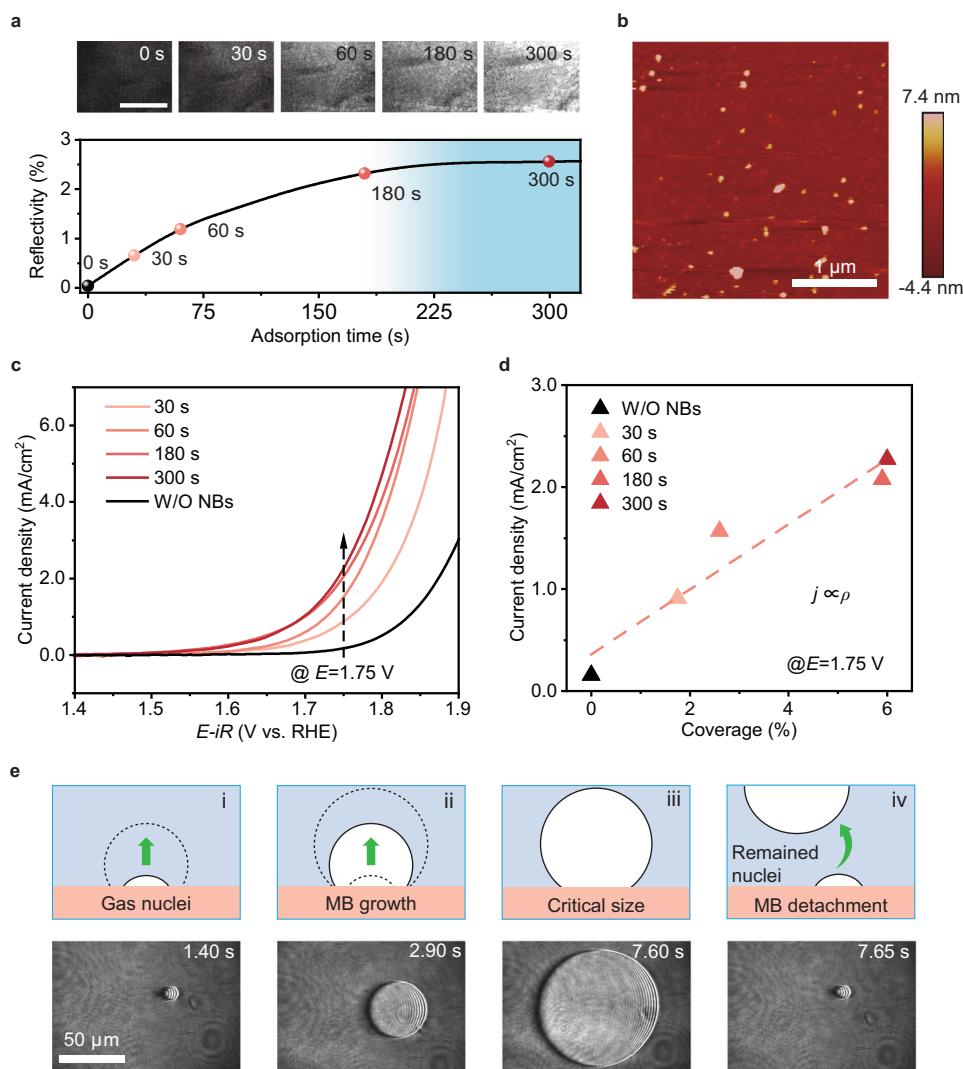


Fig. 2 | Effect of nanobubble coverage on the onset potential of OER. a Time-dependent reflectivity variation with NBs' adsorption, top: differential images of surface plasmon resonance at 0, 30, 60, 180, and 300 s (Scale bar = 400 μm). **b** Atomic force microscopy image of the electrode surface ($3 \times 3 \mu\text{m}^2$) with adsorption of NBs after 300 s. **c** OER Polarization curves of the Pt/Au electrodes ($1 \times 1 \text{cm}^2$) with different NBs' adsorption time (colored) and without NBs' adsorption (black) (with 100% iR correction and $R_s = 3.73 \pm 0.108 \Omega$). The non- iR corrected

voltammograms are provided in Supplementary Fig. S30). **d** Plots of current density (statistically derived from (c)) and NB coverage at 1.75 V vs RHE. **e** In situ surface plasmon resonance microscope (SPRM) observation of macrobubble (MB) formation/detachment and the remaining gas nuclei. Source data for (a, c, d) are provided as a Source Data file. For further details of (e), we refer to Supplementary Movie 1.

essentially a certain value owing to the surface wettability of a given electrode^{57,58}. As a result, as long as the size of introduced bulk NBs is determined, the footprint diameter or the initial curvature radius (r_0) is also determined (Fig. 3d, black line), and the critical curvature radius (r_c) is accordingly determined as with the given critical contact angle (orange line). Hence, larger-sized NBs adsorbed on the electrode surface would get larger r_c , namely, lower supersaturation required (lighter background color), corresponding to earlier transformation.

Verification of NB gas species

To further investigate the versatility of such NB additive strategy, other specific gas NBs were evaluated for OER and HER tests. Specifically, a series of gas species, including N_2 , H_2 , O_2 , and air NBs, were introduced into the electrolyte for OER. After the adsorption of NBs reached equilibrium (>5 min), LSV tests were performed. As shown in Fig. 4a, it can be seen that the presence of nitrogen, oxygen, and air NBs can lead to lowered onset potentials as compared with the solution without NBs (black line). Whereas H_2 -saturated solution and H_2 NBs solution lead to

enlarged onset potential for OER. A similar situation can be observed for HER (Fig. 4b), where solutions containing H_2 , N_2 , and even air NBs exhibit a promotion effect, while the introduction of O_2 -saturated and O_2 NBs solutions causes a negative effect. It is reasonable that the introduced target or reaction-inert gas species (e.g., H_2 or N_2 for HER, O_2 or N_2 for OER) would promote the MBs' formation, but the negative effect of reaction-interfering gas species (e.g., O_2 for HER, H_2 for OER) should be relative to the side reactions (ORR or HER).

In order to trace the variations on the cathode, we conducted the in situ SPRi observations for the HER with and without introducing O_2 NBs. As shown in Fig. 4c, the reflectivity initially increases from 0 to -2.41% till 400 s owing to the absorption of O_2 NBs. Strikingly, there is an obvious decrease in the reflectivity after 411 s at which the HER potential (-0.01 V vs RHE) is applied, indicating the consumption of adsorbed O_2 NBs. After 470 s, the reflectivity gradually increases, but the increasing rate (slope) at that time are much lower than that of the intrinsic nucleation without the introduction of O_2 NBs (as marked with blue dashed line in Fig. S12a), which clearly indicated the negative

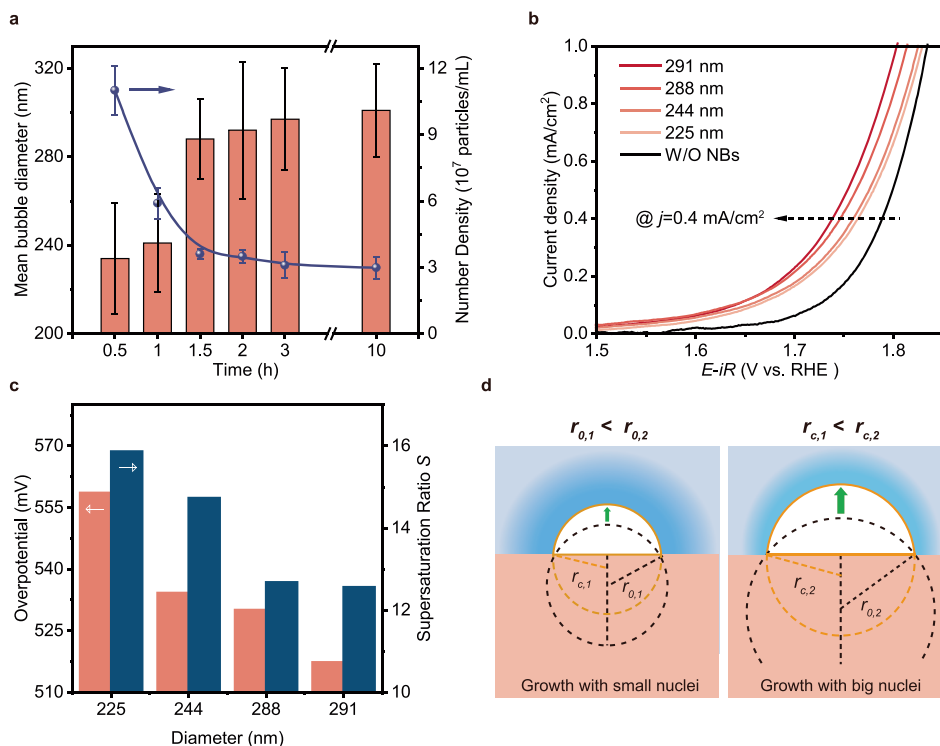


Fig. 3 | Effect of nanobubble size on the onset potential of OER. a Time-dependent variation of oxygen NB diameter and number density within 10 h. **b** OER polarization curves of the Pt/Au electrodes ($1 \times 1 \text{ cm}^2$) with different size NBs' adsorption (colored) and without NBs' adsorption (black) (with 100% iR correction and $R_s = 3.72 \pm 0.183 \Omega$). The non- iR corrected voltammograms are provided in

Supplementary Fig. S30. **c** The OER overpotential at 0.4 mA/cm^2 is statistically derived from (b) and the corresponding calculated supersaturation ratio S of the adsorbed NBs with different sizes. **d** Schematic illustration of the difference in the transformation from NBs to MBs with small (left) and big (right) nuclei. Source data for (a–c) are provided as a Source Data file.

influence of O_2 NBs-introduced HER polarization curves (Fig. 4b). Apart from the oxygen reduction reaction induced bubble removal, we suspect that the adsorbed O_2 NBs and electrogenerated H_2 NBs could constitute a pair of reactive gas species, exhausted by the highly catalytic Pt surface upon bubble coalescence⁵⁹. As a result, the cavities would get wetted and eliminated for new NBs' nucleation and bringing an extra nucleation energy barrier. In other words, such phenomena of the area wetting induced by the side reactions would cause the deactivation of NBs' nucleation sites (Fig. 4d), and require extra overpotential for re-nucleation. Taking the above observations into account, the full separation of produced gas bubbles in electrolyte during electrolysis should be of great significance for the start-up of water electrolysis devices, as the mixed NBs would induce extra energy consumption owing to the bubble removal effect, which has always been neglected before.

Application for a water splitting device with repeated start-stop operations

To further verify the NB addition strategy for the adaptation of the power fluctuations of renewable (wind and solar) energy in practical scenarios (Fig. 5a), we applied it in an anion exchange membrane (AEM) water splitting device (Fig. S13) as a probe system, with nickel-iron layered double hydroxide (NiFe-LDH) as anode (Figs. S14 and S16) and NiMo (Figs. S15 and S17) as cathode. With Ar NBs as the additive, the constant current density was set as 200 mA/cm^2 and the duration of both on and off was set as 100 s (Fig. 5b). The overall water splitting potential of the device remains stable at 1.54 V, but the scenario without introduction of NBs is 1.55 V initially (Figs. 5c and S18) and gradually increases to 1.59 V during 120 cycles of repeated start-stop operation.

The loading conditions of catalysts after tests were verified by the scanning electron microscopy (SEM) images of the working electrode

(Fig. 5d), where the catalyst layer remains intact for both NiMo and NiFe-LDH electrodes with the introduction of NBs. While there is obvious peeling off from the electrodes without NB introduction, with a considerable proportion of exposure of bare nickel foam backbone, which can also be verified by the optical image (Fig. S19). Further LSV tests reveal that electrochemical activity can be well preserved for the electrodes after cycles in the presence of NBs. Since the redox peak slightly overlaps with the OER onset potential, a negative scan with the rate of -5 mV/s was used, and the same reduction peak at -1.35 V corresponding to the reduction from Ni^{3+} to Ni^{2+} sites can be observed^{60,61}. Specifically, at a current density of 10 mA/cm^2 , the overpotentials of NiMo and NiFe-LDH electrodes are diminished by 71 and 20 mV, as compared to the ones after cycles without NBs, respectively (Fig. 5e, f). Besides, the performance degradation is also verified through the examination of double-layer capacitor (C_{DL}) and Tafel slope measurements (Fig. 5g, h). For example, the C_{DL} of the NiFe-LDH electrode, as depicted in Figs. 5g and S20, exhibits a decline from 4.40 to 3.26 mF/cm^2 after 300 cycles in the presence of NBs, which is in contrast to the sharper decrease to 2.34 mF/cm^2 for the absence of NBs. Similarly, the Tafel slope of the NiFe-LDH electrode after 300 cycles without NBs escalates from 58.86 to 80.32 mV/dec . Conversely, for the electrode after cycles operated in the presence of NBs, the Tafel slope remains almost constant at 60.69 mV/dec (Fig. S21), indicative of sustained electrochemical activity.

Besides, steady-state operation was also conducted using the same AEM configuration. The addition of Ar NBs to the electrolyte exhibits beneficial effects in terms of reducing the operating voltage and decreasing the decay rate of performance (Fig. S24). In detail, the operation voltage of the AEM device without the introduction of Ar NBs is 1.738 V initially, and increases to 1.845 V during -38 h operation time. In comparison, the operation voltage in the presence of Ar NBs is 1.701 V at start, and increases to 1.779 V at the end of operation. The

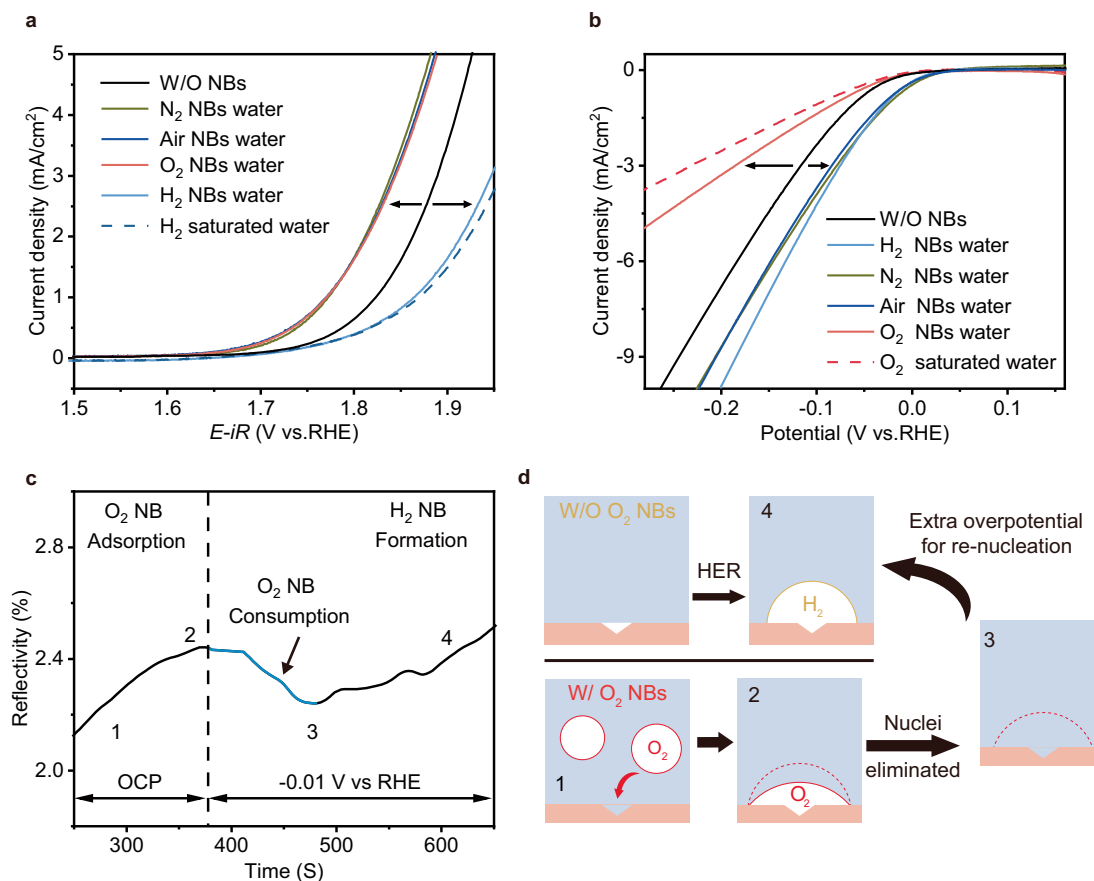


Fig. 4 | Verification of gas species for the promotion of MBs. a OER Polarization curves of Pt/Au electrode ($1 \times 1 \text{ cm}^2$) with different gas species (with 100% iR correction and $R_s = 3.63 \pm 0.33 \Omega$). **b** HER Polarization curves of Pt/Au electrode ($1 \times 1 \text{ cm}^2$) with different gas species (with 100% iR correction and $R_s = 3.49 \pm 0.249 \Omega$). **c** Time-dependent reflectivity variations of Pt/Au electrode with O₂ NBs

adsorption, where OCP refers to open circle potential and the black dashed line denotes the start of given potential (-0.01 V vs RHE). **d** Schematic illustration of the plausible mechanism for the cathodic H₂ seed removal in the presence of O₂. Note: The non- iR corrected LSV curves of 4A and 4B are provided in Supplementary Fig. S30. Source data for (a–c) are provided as a Source Data file.

rate of voltage rise is 2.82 mV/h without Ar NBs and would decrease to 2.05 mV/h in the presence of Ar NBs. The beneficial effects can also be verified by the polarization curves (Fig. S25), as the presence of Ar NBs brings 14 mV voltage decrease at a current density of 1A/cm² compared to that without Ar NBs.

To exclude possible gas crossover induced by the addition of NBs with cathodic H₂ and anodic O₂ species, an AEM device (for its superior capability against gas crossover) was chosen with Ar NBs as an additive to fully demonstrate the solely “NB effect” in the above experiments. Nonetheless, we also provide experimental results by using the H-cell with commercial Zirfon membrane. As shown in Fig. S26, the addition of NBs (injection of O₂ NBs into O₂ generating half-cell and H₂ NBs into H₂ generating half-cell) can lead to 89 and 11 mV promotion effect (at 3 mA/cm²) even against high solution resistance (14.71 Ω). Besides, all the results, including the addition of Ar or H₂ NBs to the cathode half-cell, and O₂ or Ar NBs to the anode half-cell, exhibit stable operation voltage during repeated start-stop cycles (Fig. S27). With both H₂ and O₂ NBs as additives, the operating voltage at 50 mA/cm² during repeated start-stop cycles is almost unchanged (10 mV after 400 cycles) compared to the voltage increase of 132 mV of the operation without NB introduction (Fig. S28).

Energy comparison indicates that the energy input for NB generators (ca. 72 kWh) operating during the start-up stage is almost negligible (0.047%) compared to the energy consumption by the electrolyzer (ca. 152,000 kWh for a 38 kW electrolyzer) (Note S3). Thus, by using NBs with targeted gas species, we created

a scenario in which our NB additive strategy is traceless and would not interfere with the product purity (therefore, it would be rather easy to couple with the modern water splitting device). As further verified by the NB concentration measurement, the NBs do not process the ability to cross Zirfon membrane, since no obvious increase in NB concentration can be observed in the anode half-cell when NBs are present in the cathode half-cell for 6 h (Fig. S29 and Table S1), ensuring the strategy safety when applied. Altogether, these results demonstrate that the introduction of NBs can effectively stabilize the operation condition without crossover risk, which is also helpful for extending the lifetime of the catalyst during the repeated start-off operations.

In conclusion, we propose a traceless “bubble-seeding” strategy by introducing target (H₂ and O₂) or inert (N₂) NBs into the electrolyte to promote the generation of MBs. The adsorbed NBs on the electrode surface can work as the beforehand nuclei with a certain supersaturation, and lower the supersaturation barrier for MBs’ growth, resulting in reduced overpotential. With the introduction of NBs, the operation voltage of the AEM device during repeated start-stop cycles can be stabilized within 120 cycles, indicating great potential for water electrolysis applications using renewable fluctuating energy supply. Such traceless NB additive strategy paves an alternative way for devices themselves to adapt fluctuating renewable energy, and more importantly, promotes the performance from another perspective from bubble engineering besides the traditional efforts toward catalyst optimization.

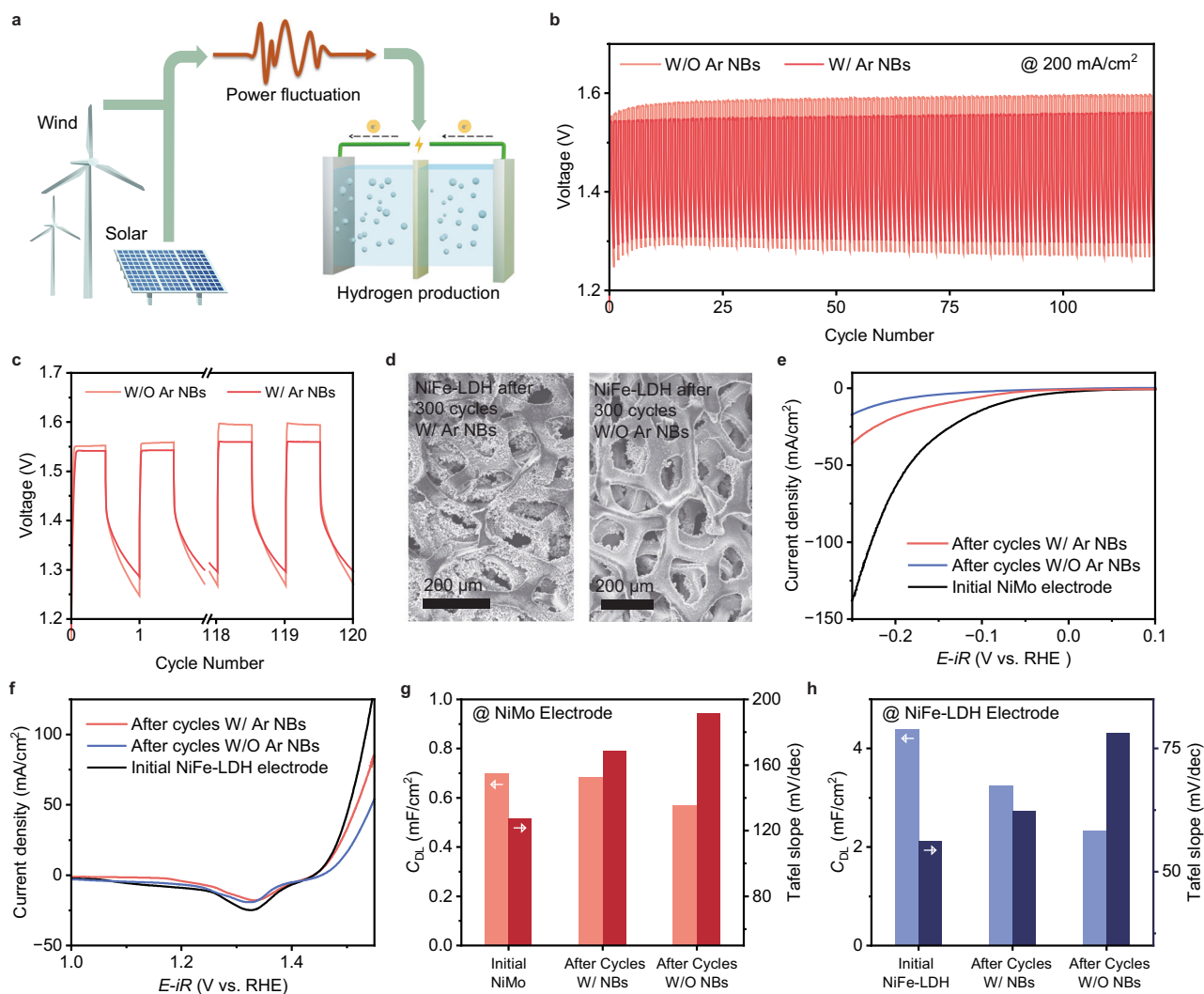


Fig. 5 | Application for a water splitting device with repeated start-stop operation. **a** Scheme of the power fluctuations of renewable (wind and solar) energy for hydrogen production devices. **b** Repeated start-stop cycles performance of the AEM device with/without the introduction of Ar NBs to keep the current density of 200 mA/cm². **c** Voltage variation during repeated start-stop test with/without the introduction of Ar NBs. **d** SEM images of the NiFe-LDH electrode after repeated start-stop cycle tests with and without NBs. **e** HER polarization curves of the as-prepared NiMo electrode (black) and after 300 cycles of repeated start-stop operation with Ar NBs (red) and without NBs (blue) (with 100% *iR* correction and $R_s = 0.89 \pm 0.050 \Omega$). **f** OER polarization curves of the as-prepared NiFe-LDH

electrode (black) and after 300 cycles of repeated start-stop operation with Ar NBs (red) and without NBs (blue) (with 100% *iR* correction and $R_s = 0.84 \pm 0.120 \Omega$). **g** C_{DL} and Tafel slope of the freshly prepared NiMo electrode (Initial NiMo) and NiMo electrode after repeated start-stop cycles operation with NBs (After Cycles W/ NBs) and without NBs (After Cycles W/O NBs). **h** C_{DL} and Tafel slope of the freshly prepared NiFe-LDH electrode (Initial NiFe-LDH) and NiFe-LDH electrode after repeated start-stop cycles operation with NBs (After Cycles W/ NBs) and without NBs (After Cycles W/O NBs). Note: The non-*iR* corrected LSV curves of SE and SF are provided in Supplementary Fig. S31. Source data for (b, c, e–h) are provided as a Source Data file.

Methods

Chemicals and materials

All aqueous solutions were prepared using DI water with a conductivity of 18.2 M Ω ·cm⁻¹ from a Heal Force water purification system. Hydrochloric acid (37%), (NH₄)₆Mo₇O₂₄·4H₂O (99%), potassium hydroxide (95%), and silicon wafers (99.999%) were purchased from Aladdin Shanghai. Ni(NO₃)₂·6H₂O (99%), Urea (99.5%), and Fe(NO₃)₃·9H₂O (99%) were obtained from Alfa Aesar. Acetone (99%) and ethanol absolute (99.9%) were purchased from Beijing Chemical Reagent Factory. Gold particles (99.99%) and chrome rods (99.99%) were purchased from Shanghai Hao Chen Co. Nickel foam was purchased from Shanxi Li Zhiyuan Battery Materials Ltd. Pt plates and all reference electrodes were purchased from Beijing Union Trust Technology Co., Ltd. All chemicals were used as received.

Preparation of electrolyte with/without bulk NBs

A micro and nanobubble generator (YC-WNM-Q3-03, U-Tron Environmental Technology Co.) was used to prepare bulk NBs with a gas inlet of 100 mL/min. After 30 min, potassium hydroxide solution (5 M) was added into the bulk NB solution to adjust the solution pH to be 13 (± 0.02) or 14 (± 0.02) using a pH meter (BPH-7100C, BELL Analytical Dalian Instruments Co., Ltd). For electrolytes without bulk NBs, the procedures were identical except that DI water was used instead of NB solution. The as-prepared electrolyte was either used immediately after preparation or stored in a glove box. The NB concentration was confirmed via NTA device (NS500, Malvern Instruments Ltd).

Preparation of Pt/Au electrode

The silicon wafers were immersed in acetone for 30 min with ultrasonication, then rinsed with water to remove any contamination. A

3 nm thick chromium and a 47 nm thick film were deposited on the surface of the clean silicon wafers using a vacuum hydro-evaporator (MB-ProVap 3G, MBRAUM). Finally, a high-vacuum coater (LEICA EM SCD 500) was used to spray Pt on the wafer for 30 s. The prepared electrode is denoted as a Pt/Au electrode.

Preparation of NiFe-LDH electrode

NiFe-LDH electrodes were prepared by a hydrothermal method. First, 0.66 mmol $\text{Ni}(\text{NO}_3)_2 \cdot 6\text{H}_2\text{O}$, 0.33 mmol $\text{Fe}(\text{NO}_3)_3 \cdot 9\text{H}_2\text{O}$ and 0.5 mmol urea were dissolved in 36 mL DI water to form a clear solution. Nickel foam (about 5×2 cm) was immersed in concentrated HCl solution (37 wt%) in an ultrasound bath for 5 min to remove the surface nickel oxide layer, and then washed by deionized water and ethanol, respectively, for 5 min to remove the remnant acid. The solution and the nickel foam were transferred to a 40 mL Teflon-lined stainless-steel autoclave, which was sealed, maintained at 120 °C for 12 h, and then allowed to cool to 25 °C naturally. A brown NiFe-LDH nanoarray was formed and subsequently rinsed with distilled water, ethanol for 5 min, ultrasonically. The prepared NiFe-LDH was dried in the air. The catalyst loading was determined to be 4.13 ± 0.606 mg/cm² (4 independent measurements) by measuring the mass difference before and after the hydrothermal process.

Preparation of NiMo electrode

NiMo electrodes were prepared by a two-step method. First, a piece of Ni form (23×30 mm) was cleaned with ethanol, 3 M HCl, and deionized water for 20 min, respectively. 10 mM $(\text{NH}_4)_6\text{Mo}_7\text{O}_{24} \cdot 7\text{H}_2\text{O}$ and 40 mM $\text{Ni}(\text{NO}_3)_2 \cdot 6\text{H}_2\text{O}$ were added to deionized water (60 mL) and stirred to form a uniform solution. Finally, the cleaned Ni form was transferred to a Teflon-lined stainless-steel autoclave (80 mL), maintained at 150 °C for 6 h to grow NiMoO₄ on the Ni form. The sample was taken out of the autoclave and rinsed with deionized water and ethanol. The sample was dried in an oven at 60 °C and then placed into a quartz tube furnace and heated to 500 °C with heating rate of 5 °C·min⁻¹ under H₂/Ar atmosphere (5 vol.% H₂ + 95 vol.% Ar). After thermal reduction for 2 h, the resulting product was denoted as NiMo electrode. The catalyst loading was determined to be 17.55 ± 3.129 mg/cm² (4 independent measurements) by measuring the mass difference before and after the hydrothermal process.

Characterization of Pt/Au electrode

SEM was performed using a Zeiss SUPRA 55 microscope to investigate the surface morphology of Pt/Au silicon wafers. The dispersion of platinum and gold elements on the electrode surface was analyzed by elemental energy spectroscopy (GENESIS XM), and the roughness of the electrode surface was characterized by AFM (Keysight 5500 ILM).

Characterization of surface nanobubbles

SPRi (Horiba) was used to characterize the adsorption behaviors of NBs. Briefly, polarized incident light was directed onto the Pt/Au film via a BK7 quartz prism. The Au-coated prism was beforehand deposited with Pt to ensure the same chemical environment as the electrochemical tests. To avoid any signal fluctuation, the observation cell was firstly filled with 0.5 mL of water. After the background signal was stable, 2.0 mL NBs solution was injected into the cell, and the reflectivity variations were recorded as well as the differential images at different NB adsorption times. AFM (Bruker catalyst) tapping mode in liquid was used to characterize the geometry of surface NBs after an adsorption time longer than 300 s.

Setup of surface plasmonic resonance microscopy (SPRM)

The SPRM setup consists of an inverted microscope (Nikon T12-E, Japan) equipped with a 100× (NA 1.49) oil immersion objective. A 660 nm-wavelength P-polarized laser generated by a fiber-coupled super

luminescent light-emitting diode (SLED, QSDM-68002, Qphotonics) was directed onto the sensor chip surface to excite surface plasmons on the Pt-coated Au film. Plasmonic images were recorded using a complementary camera (C13440-20CU, Hamamatsu, Japan). The Pt-coated Au glass slide was used as the working electrode with Pt wire as the counter electrode and Ag/AgCl as reference electrode, constituting a three-electrode setup to perform electrochemical tests with 0.1 M KOH (pH = 13 ± 0.02) as electrolyte via an electrochemical workstation (Chi 660E).

Potential scaling to RHE and ohmic resistance determination

An experimental calibration method was adopted to convert measured potential to RHE, and the corresponding equation is,

$$E_{\text{vs RHE}} = E_{\text{measured}} - E_{\text{offset}} \quad (2)$$

where E_{measured} represents the potential relative to a designated reference electrode (e.g., vs SCE). E_{offset} is an experimentally determined conversion factor, obtained by averaging the two zero-current potentials from a CV of the hydrogen evolution/oxidation reaction at a Pt rotating disk electrode (RDE). These CVs were performed in H₂-saturated electrolyte (identical to that used in the designated reaction) within the HER/HOR potential window, using a scan rate of 5 mV/s and a rotation speed of 1600 rpm. E_{offset} of Hg/HgO (in pH = 13 ± 0.02 KOH solution), Hg/HgO (in pH = 14 ± 0.02 KOH solution), Ag/AgCl (in pH = 13 ± 0.02 KOH solution), and Ag/AgCl (in pH = 1.04 ± 0.02 H₂SO₄ solution) are 0.873 V, 0.930 V, 0.960 V, and 0.257 V, respectively. The calibrated values of the reference electrodes (E_{ref}) can be calculated if the following relationship holds entirely,

$$E_{\text{offset}} = 0.0592 \times \text{pH} + E_{\text{ref}} \quad (3)$$

giving calibrated values of 0.103 V, 0.100 V, 0.190 V, and 0.195 V for Hg/HgO (in pH = 13 ± 0.02 KOH solution), Hg/HgO (in pH = 14 ± 0.02 KOH solution), Ag/AgCl (in pH = 13 ± 0.02 KOH solution), and Ag/AgCl (in pH = 1.04 ± 0.02 H₂SO₄ solution). The ohmic resistance was determined at high frequencies using electrochemical impedance spectroscopy (EIS). For HER, the EIS tests were conducted at -10 mV vs OCP, and for OER, 10 mV vs OCP.

Electrochemical tests of Pt/Au electrodes

A three-electrode system was assembled with a Pt plate as counter electrode, Hg/HgO as reference electrode, and the Pt/Au electrode as working electrode in 40 mL pH = 13 ± 0.02 NB aqueous solution/KOH solution. Electrochemical tests were performed using an electrochemical workstation (PARSA 4000). LSV curves were collected within the potential window of the designated reference electrode and reaction (e.g., 0–1 V vs Hg/HgO for OER) with a scanning rate of 5 mV/s for OER and -5 mV/s for HER. All polarization curves were corrected for iR compensation (100%) within the cell.

Electrochemical tests of NiMo and NiFe-LDH electrodes

A three-electrode system was assembled using a Pt plate counter electrode, an Hg/HgO reference electrode, and NiMo or NiFe-LDH working electrode in 75 mL of aqueous KOH solution (pH = 14 ± 0.02). Electrochemical tests were performed using an electrochemical workstation (PARS 4000). LSV curves were collected within the potential window of the designated reference electrode and reaction (e.g., 0–1 V vs Hg/HgO for OER) with a scanning rate of -5 mV/s for both OER and HER. All polarization curves were corrected for iR compensation (100%) within the cell. To determine the C_{DL} of NiMo and NiFe-LDH electrodes, CV measurements were performed at multiple scan rates. The C_{DL} value for NiMo and NiFe-LDH electrodes was obtained by plotting the average absolute current density at the open-

circuit potential against the scanning rate. The slope of this linear fit corresponds to the C_{DL} value. The Tafel slopes were derived from LSV curves at a low overpotential fitted to the Tafel equation,

$$\eta = a + b \log j \quad (4)$$

where η is the overpotential, a is the constant, b is the Tafel slope, and j is the current density.

Repeated start-stop cycles using AEM devices

First, the test cell (Au-coated Ti body) was carefully cleaned with 1 M HCl, DI water, ethanol, and DI water again and then dried in an Ar atmosphere. Both NiMo and NiFe-LDH electrode ($2 \times 2 \text{ cm}^2$) was flattened by hot press under a pressure of 6 Mpa, resulting in an average thickness to be 0.3 mm. Then, the AEM with a size of $3.5 \times 3.5 \text{ cm}^2$ and a thickness of 20 μm (PiperION-A20, Versogen) was used without processing and sandwiched between the cathode and anode, which were positioned between two bipolar plates with PTFE sealing gaskets to prevent electrolyte leakage. Finally, all components were fastened using bolts and nuts with a torque of 4 N·m. 1 L of electrolyte with/without bulk NBs ($\text{pH} = 14 \pm 0.02$) was used. The program was set in the battery test system (LANHE, CT3002K), i.e., constant current charging (800 mA) for 100 s and resting for 100 s with 300 cycles^{62,63}. All the data were not iR corrected and displayed as raw data.

Repeated start-stop cycles using H-cell devices

In this two-electrode system, a Pt plate was used as the counter electrode, and as-prepared NiFe-LDH and NiMo electrodes ($1 \times 1 \text{ cm}^2$) were used as anode and cathode for the repeated start-stop operations. A microporous membrane ($2.5 \times 2.5 \text{ cm}^2$ in size and 500 μm in thickness) was used as a separator (Zirfon UPT 500, Agfa-Gevaert N.V.) without additional treatment. Twenty milliliters of electrolyte with/without bulk NBs ($\text{pH} = 13 \pm 0.02$) were added to each compartment after the assembly of the half-cell. The program was set in the battery test system (LANHE, CT3002K), i.e., constant current charging (50 mA) for 100 s and resting for 100 s with 300 or 400 cycles. All the data were not iR corrected and displayed as raw data.

Data availability

The data generated in this study are provided in the Source Data file. Source data are provided with this paper.

References

- Li, J., Ho, M. S., Xie, C. & Stern, N. China's flexibility challenge in achieving carbon neutrality by 2060. *Renew. Sustain. Energy Rev.* **158**, 112112 (2022).
- Brauns, J. & Turek, T. Alkaline water electrolysis powered by renewable energy: a review. *Processes* **8**, 248 (2020).
- Baykara, S. Z. Hydrogen: a brief overview on its sources, production and environmental impact. *Int. J. Hydrog. Energy* **43**, 10605–10614 (2018).
- Hosseini, S. E. & Wahid, M. A. Hydrogen production from renewable and sustainable energy resources: promising green energy carrier for clean development. *Renew. Sustain. Energy Rev.* **57**, 850–866 (2016).
- Kojima, H. et al. Influence of renewable energy power fluctuations on water electrolysis for green hydrogen production. *Int. J. Hydrog. Energy* **48**, 4572–4593 (2023).
- Gernaat, D. E. H. J. et al. Climate change impacts on renewable energy supply. *Nat. Clim. Change* **11**, 119–125 (2021).
- Wang, W., Yuan, B., Sun, Q. & Wennersten, R. Application of energy storage in integrated energy systems—a solution to fluctuation and uncertainty of renewable energy. *J. Energy Storage* **52**, 104812 (2022).
- Liang, X. Emerging power quality challenges due to integration of renewable energy sources. *IEEE Trans. Ind. Appl.* **53**, 855–866 (2017).
- Zhang, W. et al. Water electrolysis toward elevated temperature: advances, challenges and frontiers. *Chem. Rev.* **123**, 7119–7192 (2023).
- Liu, L. et al. Optimizing wind/solar combinations at finer scales to mitigate renewable energy variability in China. *Renew. Sustain. Energy Rev.* **132**, 110151 (2020).
- Zhang, L. et al. Bridging innovations of phase change heat transfer to electrochemical gas evolution reactions. *Chem. Rev.* **124**, 10052–10111 (2024).
- Kempler, P. A., Coridan, R. H. & Luo, L. Gas evolution in water electrolysis. *Chem. Rev.* **124**, 10964–11007 (2024).
- Li, M., Xie, P., Yu, L., Luo, L. & Sun, X. Bubble engineering on micro-/nanostructured electrodes for water splitting. *ACS Nano* **17**, 23299–23316 (2023).
- Liu, Y., Lu, X., Peng, Y. & Chen, Q. Electrochemical visualization of gas bubbles on superaerophobic electrodes using scanning electrochemical cell microscopy. *Anal. Chem.* **93**, 12337–12345 (2021).
- Hao, R., Fan, Y., Anderson, T. J. & Zhang, B. Imaging single nanobubbles of H_2 and O_2 during the overall water electrolysis with single-molecule fluorescence microscopy. *Anal. Chem.* **92**, 3682–3688 (2020).
- Perez Sirkin, Y. A., Gadea, E. D., Scherlis, D. A. & Molinero, V. Mechanisms of nucleation and stationary states of electrochemically generated nanobubbles. *J. Am. Chem. Soc.* **141**, 10801–10811 (2019).
- German, S. R., Edwards, M. A., Ren, H. & White, H. S. Critical nuclei size, rate, and activation energy of H_2 gas nucleation. *J. Am. Chem. Soc.* **140**, 4047–4053 (2018).
- Maheshwari, S., van der Hoef, M., Rodríguez Rodríguez, J. & Lohse, D. Leakiness of pinned neighboring surface nanobubbles induced by strong gas–surface interaction. *ACS Nano* **12**, 2603–2609 (2018).
- Chen, Q., Wiedenroth, H. S., German, S. R. & White, H. S. Electrochemical nucleation of stable N_2 nanobubbles at Pt nanoelectrodes. *J. Am. Chem. Soc.* **137**, 12064–12069 (2015).
- Zhang, L. et al. Electrochemically controlled formation and growth of hydrogen nanobubbles. *Langmuir* **22**, 8109–8113 (2006).
- Chan, C. U., Arora, M. & Ohi, C. Coalescence, growth, and stability of surface-attached nanobubbles. *Langmuir* **31**, 7041–7046 (2015).
- Zhang, S. et al. Hierarchical gradient mesh surfaces for superior boiling heat transfer. *Appl. Therm. Eng.* **219**, 119513 (2023).
- Park, S. et al. Solutal Marangoni effect determines bubble dynamics during electrocatalytic hydrogen evolution. *Nat. Chem.* **15**, 1532–1540 (2023).
- Raman, A. et al. Potential response of single successive constant-current-driven electrolytic hydrogen bubbles spatially separated from the electrode. *Electrochim. Acta* **425**, 140691 (2022).
- van der Linde, P. et al. Gas bubble evolution on microstructured silicon substrates. *Energy Environ. Sci.* **11**, 3452–3462 (2018).
- van der Linde, P. et al. Electrolysis-driven and pressure-controlled diffusive growth of successive bubbles on microstructured surfaces. *Langmuir* **33**, 12873–12886 (2017).
- Sheng, S. et al. Antibuoyancy and unidirectional gas evolution by Janus electrodes with asymmetric wettability. *ACS Appl. Mater. Interfaces* **12**, 23627–23634 (2020).
- Angulo, A. E., Frey, D. & Modestino, M. A. Understanding bubble-induced overpotential losses in multiphase flow electrochemical reactors. *Energy Fuels* **36**, 7908–7914 (2022).
- Iwata, R. et al. Bubble growth and departure modes on wettable/non-wettable porous foams in alkaline water splitting. *Joule* **5**, 887–900 (2021).

30. Angulo, A., van der Linde, P., Gardeniers, H., Modestino, M. & Fernández Rivas, D. Influence of bubbles on the energy conversion efficiency of electrochemical reactors. *Joule* **4**, 555–579 (2020).
31. Vogt, H. & Balzer, R. J. The bubble coverage of gas-evolving electrodes in stagnant electrolytes. *Electrochim. Acta* **50**, 2073–2079 (2005).
32. Vogt, H. & Stephan, K. Local microprocesses at gas-evolving electrodes and their influence on mass transfer. *Electrochim. Acta* **155**, 348–356 (2015).
33. Gabrielli, C., Huet, F. & Nogueira, R. P. Fluctuations of concentration overpotential generated at gas-evolving electrodes. *Electrochim. Acta* **50**, 3726–3736 (2005).
34. Zhou, Y. et al. Tube-sponge-inspired hierarchical electrocatalysts with boosted mass and electron transfer for efficient oxygen evolution. *Adv. Mater.* **35**, e2209500 (2023).
35. Kempler, P. A., Coridan, R. H. & Lewis, N. S. Effects of bubbles on the electrochemical behavior of hydrogen-evolving Si microwire arrays oriented against gravity. *Energy Environ. Sci.* **13**, 1808–1817 (2020).
36. Zou, X. & Zhang, Y. Noble metal-free hydrogen evolution catalysts for water splitting. *Chem. Soc. Rev.* **44**, 5148–5180 (2015).
37. Xu, Y., Wang, C., Huang, Y. & Fu, J. Recent advances in electrocatalysts for neutral and large-current-density water electrolysis. *Nano Energy* **80**, 105545 (2021).
38. Shi, Z., Wang, X., Ge, J., Liu, C. & Xing, W. Fundamental understanding of the acidic oxygen evolution reaction: mechanism study and state-of-the-art catalysts. *Nanoscale* **12**, 13249–13275 (2020).
39. Upadhyay, M. et al. Three-dimensional CFD simulation of proton exchange membrane water electrolyser: performance assessment under different condition. *Appl. Energy* **306**, 118016 (2022).
40. Chen, Q., Wang, Y., Yang, F. & Xu, H. Two-dimensional multi-physics modeling of porous transport layer in polymer electrolyte membrane electrolyzer for water splitting. *Int. J. Hydrog. Energy* **45**, 32984–32994 (2020).
41. Oruc, M. E., Desai, A. V., Nuzzo, R. G. & Kenis, P. J. A. Design, fabrication, and characterization of a proposed microchannel water electrolyzer. *J. Power Sources* **307**, 122–128 (2016).
42. Zhang, Y., Zhu, X., Wood, J. A. & Lohse, D. Threshold current density for diffusion-controlled stability of electrolytic surface nanobubbles. *Proc. Natl. Acad. Sci. USA* **121**, e2321958121 (2024).
43. Gadea, E. D., Molinero, V. & Scherlis, D. A. Nanobubble stability and formation on solid–liquid interfaces in open environments. *Nano Lett.* **23**, 7206–7212 (2023).
44. Yu, J. et al. Interfacial nanobubbles' growth at the initial stage of electrocatalytic hydrogen evolution. *Energy Environ. Sci.* **16**, 2068–2079 (2023).
45. Zhou, L. et al. Ultrahigh density of gas molecules confined in surface nanobubbles in ambient water. *J. Am. Chem. Soc.* **142**, 5583–5593 (2020).
46. Lohse, D. & Zhang, X. Pinning and gas oversaturation imply stable single surface nanobubbles. *Phys. Rev. E* **91**, 31003 (2015).
47. Lei, H. et al. Promoting surface reconstruction of NiFe layered double hydroxide for enhanced oxygen evolution. *Adv. Energy Mater.* **12**, 2202522 (2022).
48. Wang, W. Imaging the chemical activity of single nanoparticles with optical microscopy. *Chem. Soc. Rev.* **47**, 2485–2508 (2018).
49. Xie, P. et al. Plasmonic imaging of spatiotemporal electrochemical bubble evolution on smooth electrodes with different wettabilities. *Adv. Mater. Technol.* **8**, 2300892 (2023).
50. Vogt, H. The concentration overpotential of gas evolving electrodes as a multiple problem of mass transfer. *J. Electrochem. Soc.* **137**, 1179–1184 (1990).
51. Leistra, J. A. & Sides, P. J. Voltage components at gas evolving electrodes. *J. Electrochem. Soc.* **134**, 2442–2446 (1987).
52. Kleinke, M. U., de Moraes, M. A. B. & Teschke, O. A new type of PTFE-covered gas evolving electrode. *J. Electrochem. Soc.* **133**, 1815–1818 (1986).
53. Janssen, L. J. J., Visser, G. J. & Barendrecht, E. Effect of molecular chlorine diffusion on theoretical potential-current density relations for chlorine evolving electrode. *Electrochim. Acta* **28**, 155–163 (1983).
54. Gao, S. et al. Ultrasensitive CCL2 detection in urine for diabetic nephropathy diagnosis using a WS₂-based plasmonic biosensor. *Nano Lett.* **24**, 5301–5307 (2024).
55. Cai, J. et al. Experimental characterization of the bubble neck formation during its growth process on a superhydrophobic surface. *Nucl. Eng. Des.* **367**, 110762 (2020).
56. Moreno Soto, Á., Prosperetti, A., Lohse, D. & van der Meer, D. Gas depletion through single gas bubble diffusive growth and its effect on subsequent bubbles. *J. Fluid Mech.* **831**, 474–490 (2017).
57. Song, B., Walczyk, W. & Schonherr, H. Contact angles of surface nanobubbles on mixed self-assembled monolayers with systematically varied macroscopic wettability by atomic force microscopy. *Langmuir* **27**, 8223–8232 (2011).
58. Zhang, L., Zhang, X., Zhang, Y., Hu, J. & Fang, H. The length scales for stable gas nanobubbles at liquid/solid surfaces. *Soft Matter* **6**, 4515 (2010).
59. Zhang, R., Gao, Y., Chen, L., Li, D. & Ge, G. Tunable gas-gas reactions through nanobubble pathway. *ChemPhysChem* **24**, e202300429 (2023).
60. Ou, Y. et al. Cooperative Fe sites on transition metal (oxy)hydroxides drive high oxygen evolution activity in base. *Nat. Commun.* **14**, 7688 (2023).
61. Dionigi, F. et al. In-situ structure and catalytic mechanism of NiFe and CoFe layered double hydroxides during oxygen evolution. *Nat. Commun.* **11**, 2522 (2020).
62. Kuang, W. et al. Self-supported Ni/Ni(OH)₂ electrodes for high-performance alkaline and AEM water electrolysis. *Adv. Energy Mater.* **15**, 2406080 (2025).
63. Lickert, T. et al. Advances in benchmarking and round robin testing for PEM water electrolysis: reference protocol and hardware. *Appl. Energy* **352**, 121898 (2023).

Acknowledgements

This work was supported by the National Key Research and Development Project (2022YFA1504000, received by X.S. and L.L.), National Natural Science Foundation of China (21935001, received by X.S., 22379005, received by L.L.), the Fundamental Research Funds for the Central Universities, and the long-term subsidy mechanism from the Ministry of Finance and the Ministry of Education of PRC. We thank Prof. Tianyu Xue from Yanshan University for the in situ SPRM testing.

Author contributions

X.-M.S. and L.L. conceived and supervised this research. S.Y. and J.Y. conducted the sample synthesis, characterizations, electrochemical measurements, and analyzed the data. B.L. assisted with the AEM assembly and testing. D.-J.Z., P.-P.X. and M.-X.L. helped with data analysis. S.Y., X.-M.S. and L.L. wrote the manuscript with the input of all authors.

Competing interests

The authors declare no competing interests.

Additional information

Supplementary information The online version contains supplementary material available at <https://doi.org/10.1038/s41467-025-61131-3>.

Correspondence and requests for materials should be addressed to Liang Luo or Xiaoming Sun.

Peer review information *Nature Communications* thanks Jacob Schneidewind, Ferdi Karadas, and the other, anonymous, reviewer(s) for their contribution to the peer review of this work. A peer review file is available.

Reprints and permissions information is available at <http://www.nature.com/reprints>

Publisher's note Springer Nature remains neutral with regard to jurisdictional claims in published maps and institutional affiliations.

Open Access This article is licensed under a Creative Commons Attribution-NonCommercial-NoDerivatives 4.0 International License, which permits any non-commercial use, sharing, distribution and reproduction in any medium or format, as long as you give appropriate credit to the original author(s) and the source, provide a link to the Creative Commons licence, and indicate if you modified the licensed material. You do not have permission under this licence to share adapted material derived from this article or parts of it. The images or other third party material in this article are included in the article's Creative Commons licence, unless indicated otherwise in a credit line to the material. If material is not included in the article's Creative Commons licence and your intended use is not permitted by statutory regulation or exceeds the permitted use, you will need to obtain permission directly from the copyright holder. To view a copy of this licence, visit <http://creativecommons.org/licenses/by-nc-nd/4.0/>.

© The Author(s) 2025